

Enzymatic Degradation of DNA Probed by *In Situ* X-ray Scattering

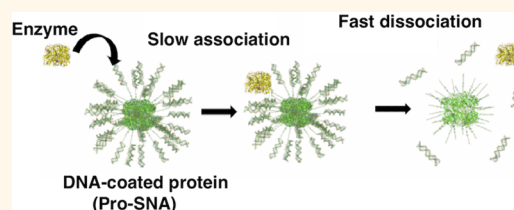
Kurinji Krishnamoorthy,^{†,‡} Sumit Kewalramani,^{‡,‡} Ali Ehlen,[†] Liane M. Moreau,[‡] Chad A. Mirkin,^{*,‡,§,||} Monica Olvera de la Cruz,^{*,†,‡,§,||} and Michael J. Bedzyk^{*,†,‡,||}

[†]Applied Physics Program, [‡]Department of Materials Science and Engineering, [§]Department of Chemistry, and ^{||}Department of Physics and Astronomy, Northwestern University, Evanston, Illinois 60208, United States

Supporting Information

ABSTRACT: Label-free *in situ* X-ray scattering from protein spherical nucleic acids (Pro-SNAs, consisting of protein cores densely functionalized with covalently bound DNA) was used to elucidate the enzymatic reaction pathway for the DNase I-induced degradation of DNA. Time-course small-angle X-ray scattering (SAXS) and gel electrophoresis reveal a two-state system with time-dependent populations of intact and fully degraded DNA in the Pro-SNAs. SAXS shows that in the fully degraded state, the DNA strands forming the outer shell of the Pro-SNA were completely digested. SAXS analysis of reactions with different Pro-SNA concentrations reveals a reaction pathway characterized by a slow, rate determining DNase I-Pro-SNA association, followed by rapid DNA hydrolysis. Molecular dynamics (MD) simulations provide the distributions of monovalent and divalent ions around the Pro-SNA, relevant to the activity of DNase I. Taken together, *in situ* SAXS in conjunction with MD simulations yield key mechanistic and structural insights into the interaction of DNA with DNase I. The approach presented here should prove invaluable in probing other enzyme-catalyzed reactions on the nanoscale.

KEYWORDS: enzymatic DNA degradation, small-angle X-ray scattering, DNA-coated proteins, molecular dynamics simulations, counterion distribution



Enzymes attack nucleic acids in cell media, thus, limiting their intracellular life times and utility as probes and gene regulation agents.¹ Therefore, probing the stability of DNA against enzymatic degradation in suitable environments would help in understanding cellular processes and in designing successful biotechnologies. Several techniques have been developed to protect and deliver nucleic acids into cells. These include packaging nucleic acids with cationic lipids,^{2,3} designing polymer-nucleic acid complexes,⁴ and functionalizing nanoparticles with nucleic acids to generate spherical nucleic acid (SNA) nanoparticle conjugates [e.g., Au-SNAs] useful for gene regulation,⁵ immunomodulation,⁶ and detection.⁷ In recent years, protein spherical nucleic acids (Pro-SNAs) have emerged as a useful class of biomaterials, composed of a functional protein core and a dense shell of covalently bound oligonucleotides.⁸ Like the prototypical Au-SNAs, Pro-SNAs exhibit efficient transfection into cells,⁸ but have the added benefit of allowing one to deliver cell-probing and therapeutic proteins.^{8–10} However, nuclease-catalyzed degradation of the oligonucleotides affects their stability and scope of use.

The activity of nucleases on free nucleic acids has been extensively studied,^{11–13} but there is limited information related to their action on SNAs. For instance, for siRNA-Au nanoparticle SNAs, the site of nuclease catalyzed hydrolysis differs from that for free siRNA.¹⁴ In addition, SNAs exhibit a half-life that is 4.3× longer than that for free DNA of the same

sequence.¹⁵ The high local counterion density and steric hindrance for the nuclease created by the dense DNA shell were hypothesized to contribute to this enhanced stability. These observations suggest the need for detailed studies focused on optimizing the design of the SNA conjugates of interest and on understanding and controlling their local ionic environment to maximize their serum stability. Furthermore, the above studies on the nuclease-mediated degradation of oligonucleotides on SNA–AuNP conjugates relied on measurements of the fluorescence intensity from fluorophore-labeled nucleic acids functionalized onto the particle core. The DNA degradation led to an enhancement of the fluorescence intensity because of the liberation of the fluorophores from the fluorescence quenching AuNP cores.¹⁶ While such fluorescence-based assays provide valuable insight into the kinetics of the reaction, they do not yield information on the structural changes occurring within the nucleic acid shell and the reaction pathway. Additionally, the fluorophore on the nucleic acids may alter the interaction between the nuclease and the nucleic acids. Here, we report a label-free structural study of the nuclease catalyzed degradation of Pro-

Received: June 17, 2019

Accepted: September 12, 2019

Published: September 12, 2019

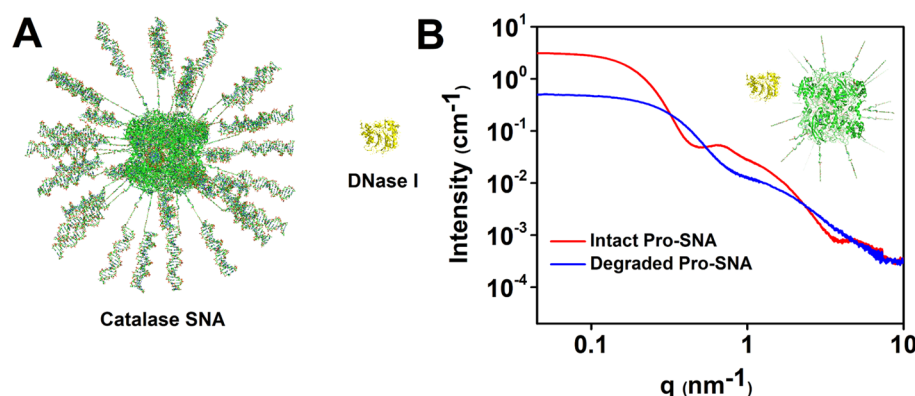


Figure 1. (A) Schematic for Pro-SNA depicting a *Cg* Catalase core ($\sim 9 \text{ nm} \times 9 \text{ nm} \times 7.5 \text{ nm}$) covalently linked with 40 ds-DNA. Also shown is the nuclease, DNase I ($\sim 4.6 \text{ nm} \times 4.2 \text{ nm} \times 3.4 \text{ nm}$), drawn to scale. (B) Background subtracted SAXS intensity profiles from Pro-SNA before (red) and after (blue) 6 h of incubation with DNase I. The intensity profile at 6 h time point (blue) was invariant over an additional 2 h of incubation with the enzyme, indicating that the degradation of Pro-SNA had completed within the first 6 h.

SNAs via small-angle X-ray scattering (SAXS).^{17,18} We will show that this ideal *in situ* nanometer scale characterization approach elucidates the reaction kinetics, as well as the structure of the intact and degraded Pro-SNA and associated DNA. Thus, revealing key mechanistic and structural insights into the enzymatic degradation of DNA functionalized onto nanoparticle cores.

Pro-SNAs are suitable candidates for SAXS measurements of DNA degradation because the monodispersed proteins and the oligonucleotides offer sufficient electron density contrast with respect to the aqueous solvent for their *in situ* structural characterization, as demonstrated by previous SAXS studies on proteins and oligonucleotides.^{19–22} Furthermore, for the case of Pro-SNAs, the comparable, yet sufficiently distinct, electron densities of the proteins and the oligonucleotides allow for a direct measurement of the spatial extension of the oligonucleotide shell.²³ In comparison, for metal nanoparticle–nucleic acid conjugates, SAXS does not yield direct structural information for the oligonucleotide shell because scattering from the very electron-dense metal cores dominates the SAXS intensity profile.²⁴ For the above reasons, we hypothesized that time-course SAXS on Pro-SNAs should sensitively probe the changes in the DNA shell during the enzymatic degradation reaction and provide time-dependent snapshots of the macroscopic state of the system to enable a deeper understanding of the reaction mechanism.

The Pro-SNA employed in this study is composed of a *Corynebacterium glutamicum* catalase (*Cg* catalase) core densely functionalized with ~ 40 DNA strands (Figure 1A). The DNA strands are covalently attached to the protein core using previously established methods.⁸ To summarize the methods, the surface accessible amines on the protein are converted into azides and then reacted with cyclooctyne (DBCO) terminated 20 base-long single-stranded DNA (ss-DNA). Complementary DNA strands are then added in excess to form double-stranded DNA (ds-DNA) on the protein surface (see Methods for details).

For the nuclease, we chose deoxyribonuclease I (DNase I), a widely distributed endonuclease in mammalian²⁵ and human tissues^{26,27} that has been previously used to test the resistance of DNA-functionalized nanoparticles to enzymatic degradation.^{16,28–32} DNase I is a glycoprotein with an average molecular mass of 30 kDa. It catalyzes the direct nucleophilic attack of the phosphorus atom on the DNA backbone by a

water hydroxyl, resulting in the cleavage of the P–O 3' bond and the formation of 5' phosphate terminated nucleotides.³³ While DNase I is not reported to have any marked sequence specificity, it preferentially cleaves phosphodiester linkages adjacent to pyrimidine bases.³⁴ Divalent Ca²⁺ and Mg²⁺ cations stabilize the conformation of DNase I and facilitate the hydrolytic cleavage of the phosphodiester bond.^{33,35,36} Consequently, the activity of DNase I is significantly reduced in buffers devoid of Ca²⁺ and Mg²⁺, or those containing high concentrations of monovalent ions.^{37–39}

For the experiments, Pro-SNAs were dispersed at concentrations varying between 0.5 and 4 μM in a DNase I reaction buffer, which contained 10 mM Tris HCl, 0.5 mM CaCl₂, and 2.5 mM MgCl₂, and had a pH of 7.6 at 25 °C. DNase I was then added to concentrations of 43–167 nM, and the reaction was allowed to proceed at room temperature for 1–6 h. The reaction mixture was sampled at intermediate time points to track changes in the scattered intensity profile. Background-subtraction was performed to isolate the scattered intensity due to Pro-SNA (protein and the attached DNA), and the degraded DNA fragments in the solution. Specifically, for the case of intact Pro-SNA dispersed in the buffer solution, background-corrected intensity profile was obtained by subtracting out the measured scattering from the capillary (sample holder) containing the reaction buffer. Similarly, for Pro-SNA–DNase I reaction mixtures, the scattering from the capillary with DNase I in the reaction buffer were subtracted out. For further details, see Methods.

X-ray scattering data was analyzed to elucidate the DNA degradation pathway, the kinetic parameters for the DNA degradation process, and to elucidate the structure of the Pro-SNA in intact and degraded states. Molecular dynamics was used to determine the ionic environment surrounding the Pro-SNA under the experimental conditions.

RESULTS AND DISCUSSION

The feasibility of SAXS for monitoring the enzymatic degradation of the DNA shell is demonstrated in Figure 1B, which shows starkly distinct background-subtracted intensity profiles from 4 μM Pro-SNA before and after 6 h of incubation with 166.6 nM DNase I. It must be noted that at this low DNase I concentration, the intensity profiles do not show any measurable features due to DNase I [section S1]. Moreover, DNase I does not affect the protein structure; over time, the

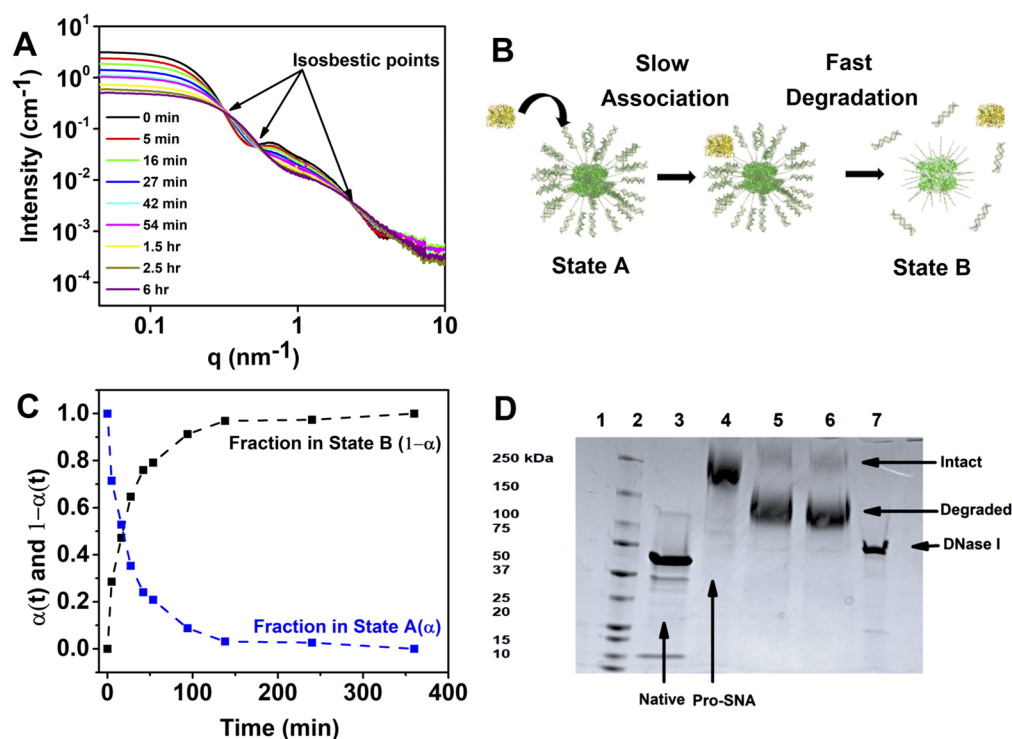


Figure 2. (A) Background subtracted SAXS intensity profiles from the $4 \mu\text{M}$ Pro-SNA, 166.6 nM DNase I system at varied time points into the reaction. The presence of isosbestic points suggests a two-state system. (B) Schematic of proposed reaction pathway consisting of a slow, rate-determining enzyme–substrate association step and a fast substrate (DNA) degradation step. (C) Time evolution of fraction of Pro-SNAs in states A (blue) and B (black), obtained by fitting time-dependent SAXS intensity profiles with eq 3. SDS PAGE gel containing a reference protein ladder (lane 2), native catalase (lane 3), Pro-SNA (lane 4), DNase I (lane 7), and Pro-SNA-DNase I reaction mixtures sampled at 30 (lane 5) and 45 min (lane 6). The resolution of the Pro-SNA into two distinct bands confirms the two-state model.

protein itself exhibits no measurable structural changes (section S2). That is, the differences in the intensity profiles (Figure 1B) are due to and qualitatively consistent with the DNase I-induced DNA degradation, as described below.

First, we show that the reduction in the forward scattered intensity [$I(q \rightarrow 0)$] (Figure 1B) is consistent with the detachment of the degraded DNA from the protein. Specifically, the background-subtracted forward scattered intensities from solutions containing the intact [$I_{\text{in}}(q = 0)$] and the fully degraded [$I_{\text{de}}(q = 0)$] Pro-SNA (e.g., the red and blue profiles in Figure 1B) include, respectively, the coherent and the incoherent sums of the forward scattering from the protein and the DNA (section S3).

$$I_{\text{in}}(q = 0) = \frac{N}{V} [(\langle \rho_{\text{prot}} \rangle_r - \rho_s) V_{\text{prot}} + N_{\text{DNA}} (\langle \rho_{\text{DNA}} \rangle_r - \rho_s) V_{\text{DNA}}]^2 \quad (1)$$

$$I_{\text{de}}(q = 0) = \frac{N}{V} \left[(\langle \rho_{\text{prot}} \rangle_r - \rho_s) V_{\text{prot}} \right]^2 + N_{\text{DNA}} \times N_f \left[(\langle \rho_{\text{DNA}} \rangle_r - \rho_s) \frac{V_{\text{DNA}}}{N_f} \right]^2 \quad (2)$$

Here, $\frac{N}{V}$ is the Pro-SNA concentration, $q = 4\pi \sin \theta / \lambda$ is the scattering vector modulus, 2θ is the scattering angle, and λ is the X-ray wavelength. $(\langle \rho_{\text{prot}} \rangle_r, \langle \rho_{\text{DNA}} \rangle_r)$ and $(V_{\text{prot}}, V_{\text{DNA}})$ are

the average electron densities and volumes for the protein and the DNA, respectively, and ρ_s is the electron density for the solvent. N_{DNA} is the number of DNA strands per protein, and N_f is the average number of fragments that each degraded DNA is divided into. On the basis of eqs 1 and 2 and the consideration that average electron densities for the protein and the DNA are higher than the aqueous solvent⁴⁰ (described later), $I_{\text{in}}(q = 0) > I_{\text{de}}(q = 0)$. That is the reduction in the forward scattered intensity after incubation with DNase I is due to a loss of spatial coupling between the protein core and the detached degraded DNA.

Second, the position of the first minimum in the intensity profiles, which is inversely related to the overall Pro-SNA size, shifts from $q_{\text{min}} \sim 0.5 \text{ nm}^{-1}$ to $q_{\text{min}} \sim 0.9 \text{ nm}^{-1}$ in going from intact to degraded Pro-SNA (Figure 1B). The reduction in Pro-SNA size is again consistent with the detachment of the whole or part of each DNA from the protein. A more quantitative analysis of the intensity profiles is described later.

Time-Dependent SAXS for Analyzing DNA Degradation Pathway. To elucidate the enzymatic reaction pathway for the Pro-SNA-DNase I system, time-course SAXS measurements were performed on $4 \mu\text{M}$ Pro-SNA incubated with 166.6 nM of DNase I (Figure 2A). The SAXS intensity profiles in Figure 2A exhibit a monotonic decrease in the forward scattered intensity [$I(q \rightarrow 0)$] with time, indicating increasing DNA degradation with time, as described above. Furthermore, the intensity profiles exhibit three clear isosbestic points at $q = 0.32, 0.54,$ and 2.2 nm^{-1} , where the measured intensity from the Pro-SNA-DNase I system is invariant during the course of the reaction. Such isosbestic points are indicative of a two-state system.^{41–46} That is, the Pro-SNA composition of the solution

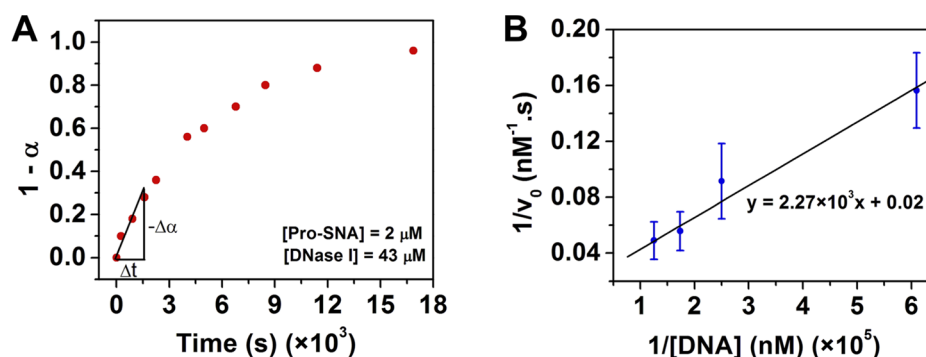


Figure 3. (A) Time-dependent fraction of degraded Pro-SNA for the case of 2 μM Pro-SNA incubated with 43 nM DNase I. (B) $1/\langle v_0 \rangle$ vs $1/[\text{DNA}]$ plot along with the best fit line. The slope and intercept of this best fit line were used to determine the rate constants k_1 and k_2 (eq 5).

at any given time is likely a linear combination of populations of intact Pro-SNA (state A, $t = 0$) and the final degraded Pro-SNA (state B, $t = 6$ h). If true, the measured intensity profile $I_t(q)$ at any intermediate time point in Figure 2A is

$$I_t(q) = \alpha(t)I_A(q) + [1 - \alpha(t)]I_B(q) \quad (3)$$

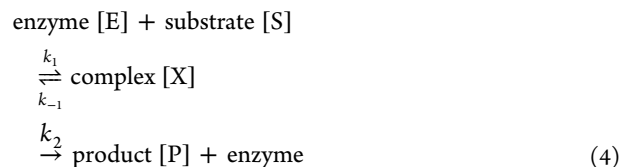
Here, I_A and I_B are the scattered intensities from the pure states A and B, respectively, and $\alpha(t)$ is the fraction of Pro-SNA that are in the intact form (state A) at a given time t . From eq 3, if $I_A = I_B$ at some specific $q = q_{\text{iso}}$, then this equality in intensity is also extended to linear combination profiles $I_t(q)$ at $q = q_{\text{iso}}$, resulting in isosbestic points observed in Figure 2A. On the basis of this two-state model, we hypothesize (and prove later) that upon association with intact Pro-SNA (state A), DNase I catalyzes a very rapid hydrolysis of the DNA shell to yield final system of degraded Pro-SNA and DNA fragments (state B), such that no intermediates are detectable (Figure 2B).

The “two-state” model is validated by two methods. First, the intensity profiles, at intermediate time points in Figure 2A, $I_t(q)$ for $0 < t < 6$ h could be described well by eq 3, using one fitting parameter per profile $\alpha(t) < 1$, which is the time-dependent fraction of the Pro-SNA in the intact form (for examples of such fits, see section S4). The fit values of $\alpha(t)$ (Figure 2C) were consistent with the expectation that $\alpha(t)$ monotonically decreases with increasing time.

To more emphatically confirm the two-state model, sodium dodecyl sulfate-polyacrylamide gel electrophoresis (SDS-PAGE) measurements were used on Pro-SNA (1 μM)-DNase I (43 nM) solutions, with reactions terminated at the 30 and 45 min time points (Figure 2D). To establish a reference, the same gel was used for simultaneous measurement on a mixture of proteins of well-known masses (lane 2), the native Cg catalase (lane 3), intact Pro-SNA (lane 4), and DNase I (lane 7). The sample pretreatment for SDS-PAGE denatures the proteins, and the SDS attachment imparts on them a high negative charge. Figure 2D shows the extent of migration of the negatively charged Protein-SDS and Pro-SNA from the top of the gel (cathode) toward the bottom of the gel (anode), after 30 min at 200 V. As can be readily observed, the two Pro-SNA-DNase I reaction mixtures sampled at the 30 min. (lane 5) and 45 min. (lane 6) time points resolve into identical sets of 3 distinct macromolecular components or bands. The macromolecules exhibiting the lowest and the highest electrophoretic mobility are identified as the intact Pro-SNAs and the DNase I through comparison with the reference samples (lanes 4 and 7). The macromolecules in the middle

band must then correspond to the degraded Pro-SNA. The degraded Pro-SNA are not identical to the native Cg catalase (Figure 2D). This is expected because even if each DNA on the Pro-SNA is completely degraded, the Pro-SNAs will retain ~ 40 bulky linkers. We note that the bands corresponding to both the intact and degraded Pro-SNA are broader than those for pure proteins. Overloading the gel columns by a high Pro-SNA concentration solution may have caused this. Alternatively, this broadening may reflect slight polydispersity in the number of DNA per protein. Further systematic experiments are required to clarify the precise origin of this broadening. Nevertheless, the separation of Pro-SNAs into two populations—intact (state A) and degraded (state B) on a SDS PAGE gel in conjunction with the above-described SAXS analysis unambiguously validates the two-state model. This implies that the macroscopic state of the Pro-SNA at any time-point in the reaction is a linear combination of fully intact and fully degraded Pro-SNA.

Deducing Reaction Kinetics via Time-Dependent SAXS. To extract the kinetic parameters that determine the DNA degradation, we analyzed time-dependent SAXS data from 0.5, 1, 1.5, and 2 μM Pro-SNA, each incubated with 43 nM DNase I (section 5) and used the Michaelis–Menten model for enzyme–substrate kinetics⁴⁷ (eq 4)



In eq 4, the enzyme (E) and substrate (S) refer to DNase I and the DNA on the protein surfaces, respectively. The above-validated two state model for DNase I catalyzed DNA degradation suggests that once a DNase I associates with a Pro-SNA, it induces a very rapid degradation of all the DNA on the Pro-SNA. Therefore, in eq 4, we assume $k_{-1} \ll k_2$. Under this assumption and for the experimental case where the DNA concentration $[S]$ ($= 20\text{--}80 \mu\text{M}$) is much higher than the DNase I concentration $[E]$ ($= 43 \text{ nM}$), the Michaelis–Menten relation can be written as

$$\frac{1}{v_0} = \frac{1}{k_2[E]} + \frac{1}{k_1[E][S]} \quad (5)$$

Here, $v_0 = \lim_{t \rightarrow 0} \frac{-d[S]}{dt}$ is the *initial velocity* or the rate of DNA decomposition in the limit $t \rightarrow 0$ and can be written as

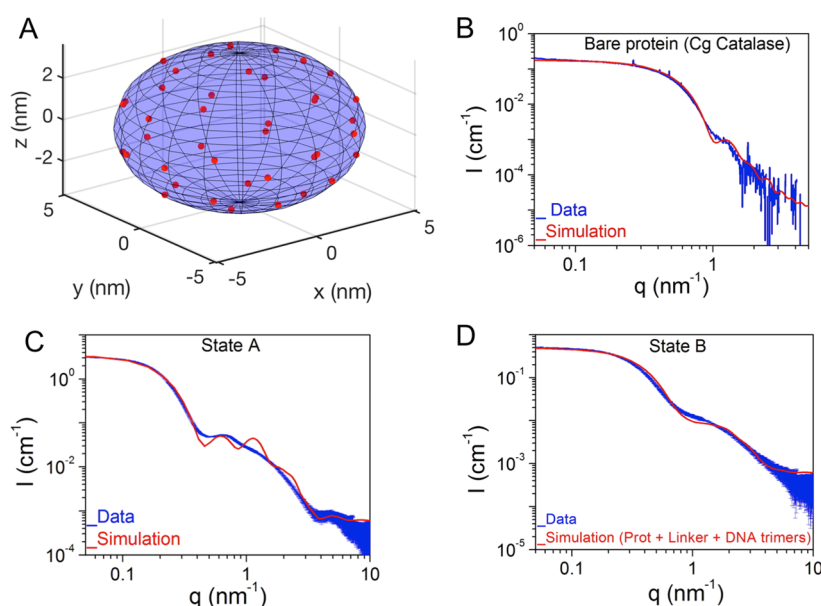


Figure 4. (A) Ellipsoid model for the protein core of a Pro-SNA showing the points of DNA attachment (red). (B) Background subtracted SAXS intensity profile of bare protein along with the simulation based on the ellipsoid model. (C and D) SAXS intensity profiles from states A (intact Pro-SNA) and B (degraded Pro-SNA + degraded DNA), along with simulation curves generated using the ellipsoid-cylinder model described in the text.

$$v_0 = -[S_0] \times \lim_{t \rightarrow 0} \frac{d\alpha}{dt} \quad (6)$$

Here, $[S_0]$ is the initial concentration of the intact DNA strands. Figure 3A shows the method of determining the rate of change in the fraction of intact Pro-SNA ($-\lim_{t \rightarrow 0} \frac{d\alpha}{dt}$), and hence, the initial reaction velocity (eq 6) for the example case of 2 μM Pro-SNA incubated with 43 nM DNase I. Here, the fraction of Pro-SNA in degraded state $[1 - \alpha(t)]$ was derived by analyzing the time-dependent SAXS data with the two-state model (eq 3), as before.

Figure 3B shows the plot of $1/\langle v_0 \rangle$ versus $1/[S]$ along with the best fit line. On the basis of eq 5, the slope and the intercept of this best-fit line yield $k_1 = (1.02 \pm 0.12) \times 10^{-5} \text{ nM}^{-1} \text{ s}^{-1}$ and $k_2 = 1.16_{-0.27}^{+0.5} \text{ s}^{-1}$, respectively. That is the rate constant for DNA degradation is 5 orders of magnitude higher than the rate constant for DNase I-DNA association: the Michaelis–Menten constant $K_M (= k_2/k_1, \text{ here}) \sim 10^5 \text{ nM}$. This agrees favorably with the lower bound of $1.4 \times 10^4 \text{ nM}$ for K_M in a previous study of DNase I-mediated degradation of a number of different short DNA.⁴⁸ We do, however, note that a fluorescence study on free DNA and DNA attached to Au nanoparticles performed at low total DNA concentrations ($\sim 20\text{--}500 \text{ nM}$) reported a $K_M \sim 400 \text{ nM}$,¹⁶ more than 2 orders of magnitude lower than the value deduced here. This discrepancy suggests the need for further detailed studies of the enzymatic degradation studies as a function of the substrate and the enzyme concentrations. Nevertheless, the result of a slow association of DNase I to DNA followed by a rapid DNA degradation appears to be valid across a range of conditions, which includes different spatial arrangements of the DNA.

Nanoscale Structural Analysis of Intact and Degraded Pro-SNA and DNA. To understand the nanoscale structural changes in Pro-SNA induced by DNA degradation, the intensity profiles from intact Pro-SNA (state A) and degraded Pro-SNA (state B) were analyzed by a simplified model. For comparison with measurements, intensity profiles

for model structures were simulated using the approach outlined in section S3. This analysis (detailed below) validates our hitherto implicit assumption that the transformation from state A to state B corresponds to DNase I induced degradation of all the DNA on the Pro-SNA. These degraded DNA consequently distribute as small fragments in the solution.

First, the Cg catalase protein core was modeled as a homogeneous ellipsoid with an electron density $\rho_{\text{prot}} = 403 \text{ e}^-/\text{nm}^3$ and semiaxes $a = b = 5.05 \text{ nm}$ and $c = 3.5 \text{ nm}$ (Figure 4A). These parameters are averages derived from the atomic-structure of Cg catalase [protein data bank (PDB ID 4B7F), see also section S6]. For the analysis of all the scattered intensity profiles, these structural parameters for the proteins were held fixed. Additionally, the electron density for the aqueous solvent was assumed to be identical to that for pure water ($\rho_s = 334 \text{ e}^-/\text{nm}^3$). A simulation based on the above ellipsoid model reproduced the measured intensity profile from the bare proteins (Figure 4B).

Second, we note that 40 DNA are tethered to the protein core, but there are 60 surface amine sites on the protein for linker and DNA attachment. To locate DNA attachment sites on the protein surface, a generalized electrostatics-based approach was adapted. We extended the Thomson problem⁴⁹ for distributing charged points on a sphere to our ellipsoidal geometry. We used a basin-hopping algorithm⁵⁰ to minimize the electrostatic potential energy associated with placing 40 unit point charges on the surface of the above-described ellipsoidal protein core (Figure 4A, red dots). At each of these sites, coupled cylinders corresponding to the linker and the DNA were attached such that the long axes of these cylinders were oriented along the ellipsoid's local surface normal. On the basis of our previous SAXS study,²³ the linker length was set to 4.0 nm. Figure 4C compares the calculated intensity profile based on the ellipsoid-cylinder model and the measured intensity profile from intact Pro-SNA (state A). The simulated profile is derived with linker and DNA radii and electron densities $(R_{\text{linker}}, R_{\text{DNA}}) = (0.75, 1.0) \text{ nm}$, $(\rho_{\text{linker}}, \rho_{\text{DNA}}) = (380,$

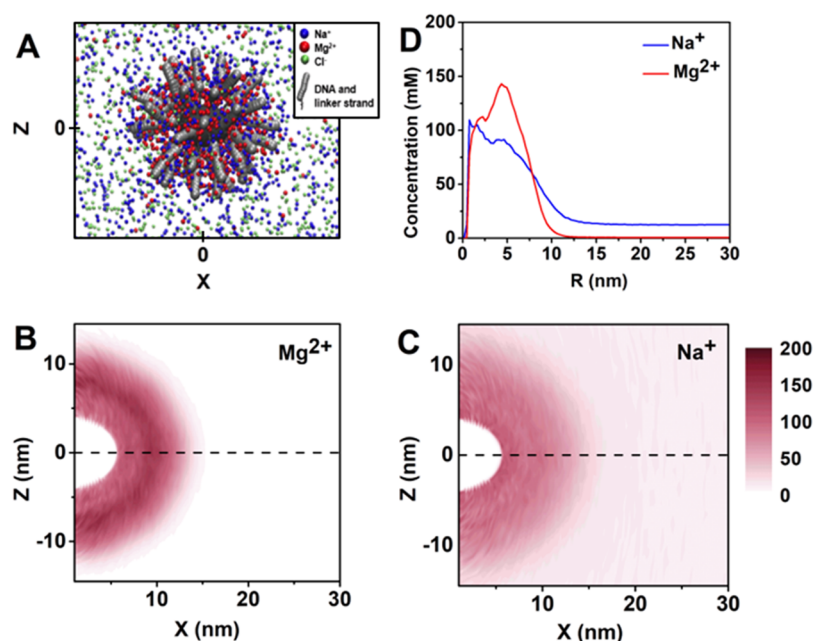


Figure 5. (A) MD simulation snapshot depicting the distribution of ions surrounding Pro-SNA. Contour maps for the angular-averaged (over the azimuthal angle ϕ) distribution of (B) divalent (Mg^{2+}) and (C) monovalent (Na^+) counterions surrounding the Pro-SNA. The color scale for ionic concentration in mM that is common to both B and C is placed at bottom, right. (D) Concentration profiles of Na^+ (blue) and Mg^{2+} (red) as a function of distance R from the surface of the protein.

440) e^-/nm^3 , and DNA length $L_{\text{DNA}} = 5.0$ nm. Apart from exhibiting sharper intensity modulations, the simulated intensity profile closely matches the overall shape, including the positions of the extrema in the measured intensity profile (Figure 4C). In particular, we note that the maximum at $q \sim 0.7 \text{ nm}^{-1} \sim 2\pi/(L_{\text{linker}} + L_{\text{DNA}})$ reflects the total length of the DNA and the linker, and the modulation with minimum at $q \sim 3.8 \text{ nm}^{-1}$ is due to the DNA cross-section (for details, see Figure S8). The scattering profile from degraded Pro-SNA (state B) can also be adequately described by using the same radii and electron densities for the DNA and the linkers (Figure 4D), but in this case all the DNA were (1) detached from the Pro-SNA and (2) divided into fragments of length $L_f = 1.0$ nm and dispersed in the solution. This fragment length roughly corresponds to 3 base pairs (trimers) in the B-DNA conformation (see also Figure S9). The division of DNA into smaller fragments was also verified by mass spectrometry analysis of the degraded Pro-SNA solution (section S7). We note that our Lego-like Pro-SNA model consisting of monodispersed linker and DNA cylinders tethered to an ellipsoid protein is a very simplistic representation of the complex Pro-SNA structure. In reality, the linker, DNA and the protein have nonuniform electron densities, the flexible linker may have a statistical distribution of sizes, and the linker and DNA axes may exhibit a range of tilts with respect to the protein surface normal. As a result, our simplified model yields much sharper modulations in the calculated scattered intensity profiles, especially for the case of intact Pro-SNA (Figure 4C). For a more detailed discussion and other model-dependent and model-independent analysis of the scattering profiles, see section S8. Nevertheless, the simplified analysis shows that the differences in the scattered intensity profiles from solutions containing intact and degraded Pro-SNAs are consistent with DNase I-mediated complete degradation of all the DNA on a Pro-SNA.

Molecular Dynamics Simulations for Distribution of Ions Surrounding Pro-SNA.

A previously referenced fluorescence study¹⁶ on DNase I-mediated degradation of DNA-AuNP conjugates suggested that the ionic environment associated with the highly charged DNA-functionalized nanoparticles significantly impacts the DNase I activity. On the basis of the indirect measurements on SNAs with different DNA loading densities, it was hypothesized that the higher the local concentration of monovalent cations (e.g. Na^+), the slower the DNA degradation rate.¹⁶ As a first step toward understanding the correlation between the local ionic environment and the rate of degradation of DNA on nanoparticles, we use molecular dynamics (MD) simulations to quantify the distribution profiles of counterions surrounding intact Pro-SNA under our experimental conditions. As previously noted, the aqueous solution in experiments contained 10 mM Tris-HCl, 0.5 mM CaCl_2 and 2.5 mM MgCl_2 ; these conditions were approximately represented in the MD simulation. On the basis of the input 10 mM Tris-HCl concentration, the pK for Tris-HCl, and a pH of 7.6, the effective Tris- H^+ concentration used was 7.52 mM. Additionally, to maintain the electroneutrality of the system, we further added 6.88 mM monovalent cations to compensate the negative charge of $4 \mu\text{M}$ Pro-SNA. Taken together, the simulation represented one Pro-SNA functionalized with 40 linker-DNA strands (20 DNA base pairs each) in implicit solvent and a total of 14.40 mM of monovalent cations, 3 mM of divalent cations, and 13.52 mM of monovalent anions, all explicitly represented using the properties of Na^+ , Mg^{2+} , and Cl^- , respectively (Table S2). The Pro-SNA model consisted of an ellipsoid with flexible chains of coarse-grained beads representing the linker-DNA strands, as shown in Figure 5A. This model is similar to that used in the analysis of X-ray scattering profiles (Figure 4A and associated text). The only difference was that instead of rigid cylinders, the linkers and the DNA were modeled as chains

with more detailed degrees of freedom (for details, see section S9).

The primary output of interest from the MD simulation is the ionic profiles surrounding the Pro-SNA. Figure 5 shows these as heat maps of the distribution of divalent (Figure 5B) and monovalent (Figure 5C) cations, averaged over the azimuthal angle ϕ . The regions of high concentrations of cations correspond closely to the shell of DNA surrounding the protein. For easier comparison of the relative concentration of the two cationic species, Figure 5D shows their angle-averaged (over θ , ϕ) concentration profiles as a function of distance (R) from the protein surface. MD simulations show that the highest azimuthally averaged concentrations of mono- and divalent cations within the DNA shell are approximately 109 and 143 mM, respectively (Figure 5D). Furthermore, within the volume of the DNA shell, the Pro-SNA charge is compensated $\sim 31\%$ and $\sim 69\%$ by mono- and divalent cations, respectively. Thus, MD results predict that despite a nearly $4.8\times$ higher concentration of monovalent cations in the solution, the counterion cloud surrounding a Pro-SNA contains a higher number of divalent cations ($\sim 48\%$ monovalent and $\sim 52\%$ divalent). In fact, in the proximity of DNA strands, the fraction of divalent cations is even higher: $\sim 70\%$ (Figure S11). We note that with such a counterion distribution, the bulk mono- and divalent cation concentrations are reduced to 12.6 mM (originally 14.4 mM) and only 0.738 mM (originally 3.0 mM), respectively (Figure 5D).

This large fraction of divalent cations in the neighborhood of DNA and in the whole shell on average is qualitatively expected: the association of one divalent cation with the Pro-SNA releases two monovalent cations in the solution, resulting in an increase in the entropy of the system. At the same time, the spatial invariance of electrochemical potential for each cation type requires some divalent cations to remain distributed in the bulk solution, and a sufficiently large number of monovalent ions to be distributed in the Pro-SNA shell (for details, see Figure S11 and associated text). From the perspective of the enzymatic reaction, the large number of divalent counterions in the DNA shell on a Pro-SNA should support the catalytic function of DNase I, leading to DNA degradation. The MD-predictions for the distribution of cations surrounding Pro-SNA can be experimentally verified using anomalous small-angle X-ray scattering (ASAXS). We have previously utilized ASAXS successfully for the case of monovalent cation-Pro-SNA system.²³ Our future ASAXS studies will quantify the distribution profiles of mono- and divalent cations surrounding Pro-SNA at varied concentrations of ions, including those relevant to the biological applications of Pro-SNA. Coupling with X-ray scattering studies on enzymatic degradation of DNA on Pro-SNA under identical conditions will allow us to correlate the rate constants for DNA degradation and the local ionic environment.

CONCLUSIONS

Label-free solution X-ray scattering in conjunction with gel electrophoresis, mass spectrometry and MD simulations was used to quantitatively track the DNase I-mediated degradation of DNA-based Pro-SNAs. X-ray scattering and gel electrophoresis show that at any time point in the reaction, the Pro-SNAs exist in either intact or fully degraded states. Analysis of X-ray scattering profiles reveals that the origin of this two-state system lies in a reaction pathway consisting of a rate determining slow DNase I-Pro-SNA association, proceeded

by a very fast degradation of all the DNA on the Pro-SNA. In particular, the rate constant for the DNase I-mediated DNA degradation is ~ 5 orders of magnitude higher than the rate constant for DNase I-DNA association. X-ray scattering and mass spectrometry show that in the fully degraded Pro-SNA state, the degraded DNA are detached from the protein surface and dispersed in solution as small fragments. MD simulations reveal that the counterion cloud associated with the DNA shell on a Pro-SNA consists of $1.09\times$ more divalent cations than monovalent cations even though the solution had a $4.8\times$ abundance of monovalent cations, in the prototypical solution conditions used. The large number of divalent counterions in the DNA shell is expected to support the catalytic function of DNase I, leading to fast DNA degradation. Overall, our measurements and analysis yield insights into the nanoscale structure of Pro-SNA and the reaction pathway for enzyme-induced DNA degradation that are inaccessible by conventional fluorescence-based nuclease assays. The findings demonstrate that it is possible to determine the physiological stability of different DNA sequences to a variety of enzymes in different conditions by using the Pro-SNA platform, which can be designed in different configurations to access the desirable probes.

METHODS

Synthesis of Pro-SNAs. All the DNA used for this study was synthesized on an ABI 392/394 automated DNA synthesizer on controlled pore glass (CPG) supports. Two DNA sequences were synthesized: a dibenzocyclooctyne (DBCO) terminated strand that was covalently attached to the protein (sequence 5' DBCO dT-(Sp18)₂GTTCCCTCGACCTTCGACCC-3'; Sp18 refers to a hexaethylene glycol spacer) and a complementary strand used for duplexing the DBCO modified DNA on the protein (sequence 5'-GGGTCGGAAGGTCGAGGAAC-3'). All the phosphoramidites and reagents used for the DNA synthesis were purchased from Glen Research. Catalase from *Corynebacterium glutamicum* (Sigma-Aldrich, product number 02071) was modified with DNA using previously described methods.⁸ Briefly, catalase was exchanged into a bicarbonate buffer (100 mM NaHCO₃, 0.5 M NaCl, pH 9.0) using Millipore Amicon ultra centrifugal filter units, following which the surface accessible amines on the protein were converted into azides by reacting the protein with a ~ 3000 -fold excess of tetraethylene glycol linkers containing an *N*-hydroxy-succinimide (NHS) ester and an azide group on opposing termini (Thermo Scientific, catalog number: 26130). The reaction between the linkers and protein was allowed to proceed for 2 h at 25 °C while shaking at 1000 rpm on a Benchmark Multitherm shaker. The azide-labeled protein was then purified by five rounds of ultracentrifugation. The number of azide labels per protein was determined through MALDI mass spectrometry (Bruker Autoflex) by comparing the molecular weight of a native Catalase protein to that of an azide-modified protein and using the fact that each azide label adds 274 Da to the weight of the protein. The concentration of the protein was determined using UV-vis spectroscopy and the known molar extinction coefficient of the protein at 405 nm ($\epsilon_{405} = 324\,000\text{ M}^{-1}\text{ cm}^{-1}$).⁸ The azide labeled proteins were then exchanged into PBS (0.5 M NaCl) by ultracentrifugation and functionalized with DBCO terminated DNA using a cycloaddition reaction (Cu-free "click chemistry") between the azide groups on the surface of the protein and the DBCO moieties on the 5' termini of the DNA. Typical reactions contained 1 μM protein and 300 μM DNA and were allowed to proceed for 3 days at 25 °C, while shaking at 1000 rpm on a Benchmark Multitherm shaker. The unreacted DNA was removed by 10 rounds of ultracentrifugation. The number of DNA strands per protein was quantified by UV-vis spectroscopy using the known molar extinction coefficients of the protein and DNA ($\epsilon_{260} = 170\,500\text{ M}^{-1}\text{ cm}^{-1}$). To hybridize the single-stranded DNA on the protein, complementary

DNA of the indicated sequence were added to the DNA functionalized proteins at a 100-fold excess relative to the protein concentration. The DNA modified proteins were then purified and exchanged into the DNase I reaction buffer (10 mM Tris-HCl, 2.5 mM MgCl₂, 0.5 mM CaCl₂, pH 7.6) to a final concentration of 0.5–4 μ M. The DNase I used for the enzymatic degradation reactions was obtained from New England BioLabs (catalog no. M0303S). DNase I was added at a final concentration of 43–167 nM to the Pro-SNA solution just before the X-ray measurements.

X-ray Scattering Measurements. *In situ* X-ray scattering measurements were conducted at Sector 5ID-D of the Advanced Photon Source at Argonne National Lab using 15 keV X-rays. The incident flux was $\sim 10^{11}$ photons/s, and the X-ray spot size at the sample was 0.25×0.25 mm². All the measurements were performed on samples held in a 1.5 mm diameter quartz capillary, which was housed in an in vacuum flow cell to minimize air scattering. In addition, the entire beam path was also placed under vacuum. Three CCD detectors placed at different distances from the sample position allowed simultaneous collection of SAXS/WAXS data over $q \sim 0.02$ – 39.3 nm⁻¹. The incident and transmitted beam intensities were monitored by an ion chamber placed before the flow cell and a cadmium tungstate scintillating crystal followed by a pin diode embedded in the beam stop, respectively. For time course X-ray scattering measurements, DNase I was added to a sample of the Pro-SNA dispersed in the reaction buffer contained in a 1.5 mL Eppendorf tube. The tube was loaded into a sample stage. For each X-ray scattering measurement, 80 μ L of the Pro-SNA-DNase I reaction mixture was pulled up into the capillary tube. To prevent radiation damage, the samples were continuously flowed through the capillary during the measurements at a flow rate of 4 μ L/s (~ 2.25 mm/s). To improve statistics, 5 frames were collected per sample with an exposure time of 3 s/frame. All the measurements were performed at room temperature using the same capillary tube. After the measurement the 80 μ L sample was discarded and the capillary was washed thoroughly with pure water, bleach and sodium hydroxide. In between subsequent measurements from the DNase I-Pro-SNA samples, scattering from empty capillary, pure water and the reaction buffer was recorded to ensure that the background level did not change by more than 2% due to sticking of the particles to the capillary walls. The 2D SAXS patterns were converted into 1D intensity profiles through azimuthal integration while taking into account the solid-angle, flat-field transmission and polarization corrections. The patterns were also normalized according to exposure time. Depending on the sample, SAXS profiles from the capillary containing water or the buffer solution, or the buffer solution with DNase I were used for background subtraction. The data were converted to an absolute intensity scale using established procedures.⁵¹ Briefly, the intensity profiles from pure water (difference between scattering profiles from capillary with pure water and empty capillary) were fitted to straight lines. The intercept of these best fit lines was set to 0.0165 cm⁻¹, which is the absolute intensity (scattering cross section/volume) for water at 25 °C. The sample data were then scaled accordingly.

Gel Electrophoresis Measurements (SDS PAGE). For the sodium dodecyl sulfate polyacrylamide gel electrophoresis (SDS PAGE) measurements, 43 nM DNase I was added to 1 μ M Pro-SNA dispersed in the reaction buffer. After 30 and 45 min, 20 μ L of the reaction mixture was diluted with 20 μ L of Laemmli sample buffer (2 \times , Sigma-Aldrich), and dithiothreitol (DTT) was added to a final concentration of 100 mM in 50 μ L. The sample was then placed in a PCR tube and heated at 85 °C for 10 min. The DTT, SDS, and the application of heat denature the proteins and linearizes them. Samples of the native catalase protein, pure Pro-SNA, and pure DNase I were prepared in the same manner. These samples were then run on a precast 4–15% protein gel (Bio-Rad, product number 4561084) with Tris-Glycine-SDS running buffer (Sigma-Aldrich). A Precision Plus Protein Standard (Bio-Rad, product number 1610373) was loaded into the second lane of the gel, while the native catalase, intact Pro-SNA, 30 and 45 min. Pro-SNA-DNase I reaction mixtures and pure DNase I were loaded into the third, fourth, fifth, sixth, and seventh

lanes of the gel, respectively. The gel was then installed into the electrophoresis apparatus (Bio-Rad Mini-PROTEAN Tetra Cell) with a buffer dam and run at 200 V for 30 min. The gel was then washed and stained using SimplyBlue SafeStain (Thermo Fisher) and imaged on a FluorChem Q imaging system (Alpha Innotech) using Transwhite excitation and EBr emission. The focus and exposure were adjusted, and an image of the gel was acquired.

ASSOCIATED CONTENT

Supporting Information

The Supporting Information is available free of charge on the ACS Publications website at DOI: 10.1021/acs.nano.9b04752.

MD simulation movie (MOV)

X-ray scattering data from DNase I solution and from a solution containing Cg Catalase protein and DNase I, additional analysis of the measured SAXS intensity profiles, outline of the method used for obtaining the calculated intensity profiles, detailed description of the structural models for DNA and protein, mass spectrometry data from degraded DNA, and details of MD simulations with additional results (PDF)

AUTHOR INFORMATION

Corresponding Authors

*E-mail: bedzyk@northwestern.edu.

*E-mail: m-olvera@northwestern.edu.

*E-mail: chadnano@northwestern.edu.

ORCID

Chad A. Mirkin: 0000-0002-6634-7627

Michael J. Bedzyk: 0000-0002-1026-4558

Author Contributions

[†]K.K. and S.K. contributed equally to the work.

Notes

The authors declare no competing financial interest.

ACKNOWLEDGMENTS

This work was primarily supported by Department of Energy, Office of Science, Basic Energy Sciences under award number DE-SC0018093. C.A.M. acknowledges support for synthesis and characterization of the SNAs from the Vannevar Bush Faculty Fellowship program sponsored by the Basic Research Office of the Assistant Secretary of Defense for Research and Engineering and funded by the Office of Naval Research through grant N00014-15-1-0043. M.O.d.I.C. acknowledges support for computational work from the Sherman Fairchild Foundation. L.M.M. acknowledges support from the National Defense Science and Engineering Graduate fellowship program. Use of the Advanced Photon Source at Argonne National Lab was supported by DOE-BES (DE-AC02-06CH11357). SAXS experiments were performed at the APS DND-CAT 5ID-D beamline, which is supported through E. I. duPont de Nemours & Co., Northwestern University (NU), The Dow Chemical Co., and the NSF-MRSEC program (DMR-1720139). We thank Dr. Steven Weigand at Sector 5 for help with experimental setup and data reduction. SAXS experiments were also performed at APS Sector 12ID-C. We thank Soenke Seifert at Sector 12 for his assistance with the SAXS setup at Sector 12ID-C.

REFERENCES

- (1) Arber, W. DNA Modification and Restriction. *Prog. Nucleic Acid Res. Mol. Biol.* 1974, 14, 1–37.

- (2) Koltover, I.; Salditt, T.; Radler, J. O.; Safinya, C. R. An Inverted Hexagonal Phase of Cationic Liposome-DNA Complexes Related to DNA Release and Delivery. *Science* **1998**, *281*, 78–81.
- (3) Leal, C.; Bouxsein, N. F.; Ewert, K. K.; Safinya, C. R. Highly Efficient Gene Silencing Activity of siRNA Embedded in a Nanostructured Gyroid Cubic Lipid Matrix. *J. Am. Chem. Soc.* **2010**, *132*, 16841–16847.
- (4) Wu, C. N.; Li, J. H.; Wang, W. D.; Hammond, P. T. Rationally Designed Polycationic Carriers for Potent Polymeric siRNA-Mediated Gene Silencing. *ACS Nano* **2018**, *12*, 6504–6514.
- (5) Rosi, N. L.; Giljohann, D. A.; Thaxton, C. S.; Lytton-Jean, A. K.; Han, M. S.; Mirkin, C. A. Oligonucleotide-Modified Gold Nanoparticles for Intracellular Gene Regulation. *Science* **2006**, *312*, 1027–1030.
- (6) Radovic-Moreno, A. F.; Chernyak, N.; Mader, C. C.; Nallagatla, S.; Kang, R. S.; Hao, L.; Walker, D. A.; Halo, T. L.; Merkel, T. J.; Rische, C. H.; et al. Immunomodulatory Spherical Nucleic Acids. *Proc. Natl. Acad. Sci. U. S. A.* **2015**, *112*, 3892–3897.
- (7) Zheng, D.; Seferos, D. S.; Giljohann, D. A.; Patel, P. C.; Mirkin, C. A. Aptamer Nano-Flares for Molecular Detection in Living Cells. *Nano Lett.* **2009**, *9*, 3258–3261.
- (8) Brodin, J. D.; Auyeung, E.; Mirkin, C. A. DNA-Mediated Engineering of Multicomponent Enzyme Crystals. *Proc. Natl. Acad. Sci. U. S. A.* **2015**, *112*, 4564–4569.
- (9) Fu, A.; Tang, R.; Hardie, J.; Farkas, M. E.; Rotello, V. M. Promises and Pitfalls of Intracellular Delivery of Proteins. *Bioconjugate Chem.* **2014**, *25*, 1602–1608.
- (10) Torchilin, V. Intracellular Delivery of Protein and Peptide Therapeutics. *Drug Discovery Today: Technol.* **2008**, *5*, e95–e103.
- (11) Mu, D.; Hsu, D. S.; Sancar, A. Reaction Mechanism of Human DNA Repair Excision Nuclease. *J. Biol. Chem.* **1996**, *271*, 8285–8294.
- (12) Blaszczyk, J.; Tropea, J. E.; Bubunenko, M.; Routzahn, K. M.; Waugh, D. S.; Court, D. L.; Ji, X. Crystallographic and Modeling Studies of RNase III Suggest a Mechanism for Double-Stranded RNA Cleavage. *Structure* **2001**, *9*, 1225–1236.
- (13) Pan, C. Q.; Lazarus, R. A. Ca²⁺-Dependent Activity of Human DNase I and Its Hyperactive Variants. *Protein Sci.* **1999**, *8*, 1780–1788.
- (14) Barnaby, S. N.; Lee, A.; Mirkin, C. A. Probing the Inherent Stability of siRNA Immobilized on Nanoparticle Constructs. *Proc. Natl. Acad. Sci. U. S. A.* **2014**, *111*, 9739–9744.
- (15) Seferos, D. S.; Prigodich, A. E.; Giljohann, D. A.; Patel, P. C.; Mirkin, C. A. Polyvalent DNA Nanoparticle Conjugates Stabilize Nucleic Acids. *Nano Lett.* **2009**, *9*, 308–311.
- (16) Giljohann, D. A.; Seferos, D. S.; Prigodich, A. E.; Patel, P. C.; Mirkin, C. A. Gene Regulation with Polyvalent siRNA-Nanoparticle Conjugates. *J. Am. Chem. Soc.* **2009**, *131*, 2072–2073.
- (17) Li, T.; Senesi, A. J.; Lee, B. Small Angle X-Ray Scattering for Nanoparticle Research. *Chem. Rev.* **2016**, *116*, 11128–11180.
- (18) Craievich, A. F. Synchrotron SAXS Studies of Nanostructured Materials and Colloidal Solutions: A Review. *Mater. Res.* **2002**, *5*, 1–11.
- (19) Lipfert, J.; Doniach, S. Small-Angle X-Ray Scattering from RNA, Proteins, and Protein Complexes. *Annu. Rev. Biophys. Biomol. Struct.* **2007**, *36*, 307–327.
- (20) Skou, S.; Gillilan, R. E.; Ando, N. Synchrotron-Based Small-Angle X-Ray Scattering (SAXS) of Proteins in Solution. *Nat. Protoc.* **2014**, *9*, 1727–1739.
- (21) Graewert, M. A.; Svergun, D. I. Impact and Progress in Small and Wide Angle X-Ray Scattering (SAXS and WAXS). *Curr. Opin. Struct. Biol.* **2013**, *23*, 748–754.
- (22) Andresen, K.; Das, R.; Park, H. Y.; Smith, H.; Kwok, L. W.; Lamb, J. S.; Kirkland, E. J.; Herschlag, D.; Finkelstein, K. D.; Pollack, L. Spatial Distribution of Competing Ions around DNA in Solution. *Phys. Rev. Lett.* **2004**, *93*, 248103.
- (23) Krishnamoorthy, K.; Hoffmann, K.; Kewalramani, S.; Brodin, J. D.; Moreau, L. M.; Mirkin, C. A.; Olvera de la Cruz, M.; Bedzyk, M. J. Defining the Structure of a Protein-Spherical Nucleic Acid Conjugate and Its Counterionic Cloud. *ACS Cent. Sci.* **2018**, *4*, 378–386.
- (24) Kewalramani, S.; Zwanikken, J. W.; Macfarlane, R. J.; Leung, C.-Y.; Olvera de la Cruz, M.; Mirkin, C. A.; Bedzyk, M. J. Counterion Distribution Surrounding Spherical Nucleic Acid–Au Nanoparticle Conjugates Probed by Small-Angle X-Ray Scattering. *ACS Nano* **2013**, *7*, 11301–11309.
- (25) Lacks, S. A. Deoxyribonuclease I in Mammalian Tissues. Specificity of Inhibition by Actin. *J. Biol. Chem.* **1981**, *256*, 2644–2648.
- (26) Samejima, K.; Earnshaw, W. C. Trashing the Genome: The Role of Nucleases During Apoptosis. *Nat. Rev. Mol. Cell Biol.* **2005**, *6*, 677–688.
- (27) Shiokawa, D.; Tanuma, S. Characterization of Human DNase I Family Endonucleases and Activation of DNase γ During Apoptosis. *Biochemistry* **2001**, *40*, 143–152.
- (28) Zagorovsky, K.; Chou, L. Y.; Chan, W. C. Controlling DNA–Nanoparticle Serum Interactions. *Proc. Natl. Acad. Sci. U. S. A.* **2016**, *113*, 13600–13605.
- (29) Cutler, J. I.; Zhang, K.; Zheng, D.; Auyeung, E.; Prigodich, A. E.; Mirkin, C. A. Polyvalent Nucleic Acid Nanostructures. *J. Am. Chem. Soc.* **2011**, *133*, 9254–9257.
- (30) Song, L.; Guo, Y.; Roebuck, D.; Chen, C.; Yang, M.; Yang, Z.; Sreedharan, S.; Glover, C.; Thomas, J. A.; Liu, D.; et al. Terminal Pegylated DNA–Gold Nanoparticle Conjugates Offering High Resistance to Nuclease Degradation and Efficient Intracellular Delivery of DNA Binding Agents. *ACS Appl. Mater. Interfaces* **2015**, *7*, 18707–18716.
- (31) Yuan, Y.; Tan, J.; Wang, Y.; Qian, C.; Zhang, M. Chitosan Nanoparticles as Non-Viral Gene Delivery Vehicles Based on Atomic Force Microscopy Study. *Acta Biochim. Biophys. Sin.* **2009**, *41*, 515–526.
- (32) Han, G.; Martin, C. T.; Rotello, V. M. Stability of Gold Nanoparticle-Bound DNA toward Biological, Physical, and Chemical Agents. *Chem. Biol. Drug Des.* **2006**, *67*, 78–82.
- (33) Suck, D.; Oefner, C. Structure of DNase I at 2.0 Å Resolution Suggests a Mechanism for Binding to and Cutting DNA. *Nature* **1986**, *321*, 620–625.
- (34) Matsuda, M.; Ogoshi, H. Specificity of DNase I. *J. Biol. Chem.* **1966**, *59*, 230–235.
- (35) Guérout, M.; Picot, D.; Abi-Ghanem, J.; Hartmann, B.; Baaden, M. How Cations Can Assist DNase I in DNA Binding and Hydrolysis. *PLoS Comput. Biol.* **2010**, *6*, No. e1001000.
- (36) Price, P. A. The Essential Role of Ca²⁺ in the Activity of Bovine Pancreatic Deoxyribonuclease. *J. Biol. Chem.* **1975**, *250*, 1981–1986.
- (37) Melgar, E.; Goldthwait, D. A. Deoxyribonucleic Acid Nucleases II. The Effects of Metals on the Mechanism of Action of Deoxyribonuclease I. *J. Biol. Chem.* **1968**, *243*, 4409–4416.
- (38) Campbell, V. W.; Jackson, D. The Effect of Divalent Cations on the Mode of Action of DNase I. The Initial Reaction Products Produced from Covalently Closed Circular DNA. *J. Biol. Chem.* **1980**, *255*, 3726–3735.
- (39) Shack, J. Influence of Sodium and Magnesium Ions on the Action of Deoxyribonuclease II. *J. Biol. Chem.* **1959**, *234*, 3003–3006.
- (40) Putnam, C. D.; Hammel, M.; Hura, G. L.; Tainer, J. A. X-Ray Solution Scattering (SAXS) Combined with Crystallography and Computation: Defining Accurate Macromolecular Structures, Conformations and Assemblies in Solution. *Q. Rev. Biophys.* **2007**, *40*, 191–285.
- (41) Lang, J.; Maréchal, A.; Couture, M.; Santolini, J. Reaction Intermediates and Molecular Mechanism of Peroxynitrite Activation by No Synthases. *Biophys. J.* **2016**, *111*, 2099–2109.
- (42) Vinokurov, I. A.; Kankare, J. Beer's Law and the Isosbestic Points in the Absorption Spectra of Conductive Polymers. *J. Phys. Chem. B* **1998**, *102*, 1136–1140.
- (43) Dai, X.; Mashiguchi, K.; Chen, Q.; Kasahara, H.; Kamiya, Y.; Ojha, S.; DuBois, J.; Ballou, D.; Zhao, Y. The Biochemical Mechanism of Auxin Biosynthesis by an Arabidopsis Yucca Flavin-Containing Monooxygenase. *J. Biol. Chem.* **2013**, *288*, 1448–1457.

- (44) Matsudaira, P.; Bordas, J.; Koch, M. Synchrotron X-Ray Diffraction Studies of Actin Structure During Polymerization. *Proc. Natl. Acad. Sci. U. S. A.* **1987**, *84*, 3151–3155.
- (45) Perakis, F.; Amann-Winkel, K.; Lehmkuhler, F.; Sprung, M.; Mariedahl, D.; Sellberg, J. A.; Pathak, H.; Späh, A.; Cavalca, F.; Schlesinger, D.; et al. Diffusive Dynamics During the High-to-Low Density Transition in Amorphous Ice. *Proc. Natl. Acad. Sci. U. S. A.* **2017**, *114*, 8193–8198.
- (46) Helm, C.; Tippmann-Krayer, P.; Möhwald, H.; Als-Nielsen, J.; Kjaer, K. Phases of Phosphatidyl Ethanolamine Monolayers Studied by Synchrotron X-Ray Scattering. *Biophys. J.* **1991**, *60*, 1457–1476.
- (47) Leskovac, V. *Comprehensive Enzyme Kinetics*; Kluwer Academic/Plenum Publishers: New York, 2003; pp 31–49.
- (48) Sutton, D. H.; Conn, G. L.; Brown, T.; Lane, A. N. The Dependence of DNase I Activity on the Conformation of Oligodeoxynucleotides. *Biochem. J.* **1997**, *321* (2), 481–486.
- (49) Thomson, J. J. On the Structure of the Atom: An Investigation of the Stability and Periods of Oscillation of a Number of Corpuscles Arranged at Equal Intervals around the Circumference of a Circle; with Application of the Results to the Theory of Atomic Structure. *Philos. Mag.* **1904**, *7*, 237–265.
- (50) Wales, D. J.; Doye, J. P. K. Global Optimization by Basin-Hopping and the Lowest Energy Structures of Lennard-Jones Clusters Containing up to 110 Atoms. *J. Phys. Chem. A* **1997**, *101*, 5111–5116.
- (51) Fan, L.; Degen, M.; Bendle, S.; Grupido, N.; Ilavsky, J. In *The Absolute Calibration of a Small-Angle Scattering Instrument with a Laboratory X-Ray Source*, J. Phys. Conf. Ser.; IOP Publishing, 2010; p 012005.